Topological phase transitions in thin films by tuning multivalley boundary-state couplings

Xiao Li (□□) and Qian Niu

Phys. Rev. B **95**, 241411 — Published 30 June 2017

DOI: 10.1103/PhysRevB.95.241411

Topological phase transitions in thin films by tuning multivalley boundary-state couplings

Xiao Li[1] and Qian Niu[1, 2, 3]

[1]*Department of Physics, University of Texas at Austin, Austin, TX 78712, USA*
[2]*International Center for Quantum Materials, School of Physics, Peking University, Beijing 100871, P. R. China*
[3]*Collaborative Innovation Center of Quantum Matter, Beijing, P. R. China*

Dirac boundary states on opposite boundaries can overlap and interact owing to finite size effect. We propose that in a thin film system with symmetry-unrelated valleys, valley-contrasting couplings between Dirac boundary states can be exploited to design various two-dimensional topological quantum phases. Our first-principles calculations demonstrate the mechanism in tin telluride slab and nanoribbon array, respectively, by top-down and bottom-up material designs. Both two-dimensional topological crystalline insulator and quantum spin Hall insulator emerge in the same material system, which offers highly tunable quantum transport of edge channels with a set of quantized conductances.

Introduction.—Topological insulating phases, such as topological insulator and topological crystalline insulator, have important theoretical and practical implications on electronics and spintronics [1–3]. Materials discovery is crucial and challenging in the study of topological insulating phases. In particular, compared with three-dimensional counterpart, two-dimensional topological insulator, also known as quantum spin Hall insulator, has only a very few examples that have been experimentally achieved [4, 5]. Two-dimensional topological crystalline insulator was just recently predicted [6–8]. Therefore, an effective mechanism of designing two-dimensional topological quantum phases is highly desirable.

While there are few naturally occurring two-dimensional materials, two-dimensional structure can be also constructed from three-dimensional and one-dimensional systems. In this letter, we focus on such top-down and bottom-up design approaches, using two-dimensional slab and nanoribbon array as two examples. In the two structures, various two-dimensional topological quantum phases can be created by means of finite-size-induced couplings between boundary states and their valley-distinct behaviors, when there are symmetry-unrelated valleys in the momentum space.

By first-principles calculations, we demonstrate the proposed mechanism in tin telluride. Its (110) slab and nanoribbon array both have two valleys that are not related by symmetry. The boundary-states couplings in the two valleys have distinct strengths. By tuning the valley-contrasting couplings with variable film thickness and nanoribbon width as readily accessible knobs, both two-dimensional topological crystalline insulator and quantum spin Hall insulator emerge in the same material system. The resulting various two-dimensional topological phrases give rise to a dissipationless quantized transport of edge channels with multiple stepwise variations. We also discuss the possibility of the application of the mechanism in more exotic topological phases, such as Chern insulator, Majorana fermions and parafermions [9–11].

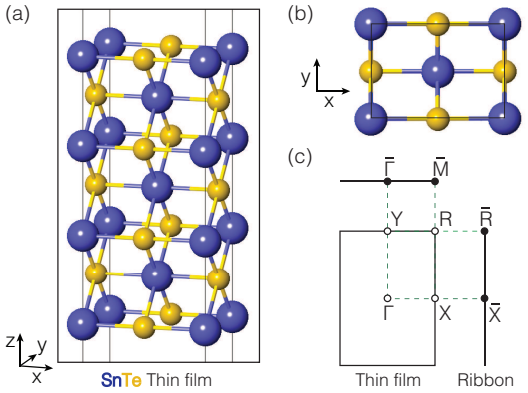

FIG. 1: Atomic structure and the Brillouin zones of (110) SnTe slab. (a) Side view and (b) top views of a representative slab, with 7 atomic layers along crystallographic [110] direction. Blue and yellow spheres stand for Sn and Te atoms, respectively. x, y and z axes are respectively along [001], [1$\bar{1}$0] and [110]. (c) The Brillouin zone of the slab and its projections along x and y directions.

Surface-state couplings in a slab.—We take SnTe film system for example to demonstrate the mechanism of valley-contrasting couplings between boundary states. We first focus on a slab cleaved from three-dimensional bulk and design two-dimensional topological phases by multiple surface-state couplings. Bulk SnTe has a rock-salt structure with (110)-like mirror planes, where two interpenetrating face-centered cubic lattices are respectively formed by tin and tellurium ions. Under the protection of mirror symmetry, bulk SnTe is a representative three-dimensional topological crystalline insulator (TCI) [12]. Its (110) slabs have two symmetry-unrelated valleys of surface states [13]. Considering that the surface-state couplings in the two valleys may behave differently, we investigate geometric and electronic properties of (110) SnTe slabs by first-principles calculations. The calcula-

tion method can be found in Supplemental Material [14]

Fig. 1 shows the structure and Brillouin zone of a SnTe slab. Each atomic layer of the slab is a rectangular lattice, with a formula unit per unit cell. There is an in-plane shift along the diagonal of the cell by a half-diagonal and equal vertical interval between two neighboring layers. Therefore, for the slabs with an odd number of atomic layers (e.g. 7 layers in Fig. 1(a)), the middle layer is a mirror plane, while the mirror is absent for even-number layers. We will focus on odd-number layers, where the presence of mirror symmetry allows of the emergence of two-dimensional topological crystalline insulator and corresponding phase transitions. Besides, the slab keeps inversion symmetry and each ionic site in the mirror plane is an inversion center.

A representative band structure of the slab is shown in Fig. 2(a). The bands are spin degenerate at each momentum, due to simultaneous time-reversal and inversion symmetries. More importantly, two symmetry-distinct valleys appear around X(π,0) and R(π,π) in the momentum space (Fig. 1(c)), where the lattice constant is used as a length unit along each direction for the coordinates. The low-energy bands of the two valleys arise from surface states of bulk SnTe [13]. For a slab of thick enough, degenerate surface states in each valley are ideally localized on two opposite surfaces, respectively. As the thickness of the slab decreases below the penetration length of surface states, an additional coupling becomes significant between surface states in the same valley but on opposite surfaces, which possibly modify low-energy bands [22, 23]. Topological phases are associated with low-energy band ordering inversions with respect to the atomic limit. Quantum spin Hall insulator (QSHI), protected by time-reversal symmetry, has an odd number of band inversions [1, 2]. In contrast, the predicted two-dimensional topological crystalline insulators, protected by mirror symmetry, have an even number of band inversions [6–8]. Considering that the two valleys in SnTe slab are not related by symmetry, we expect valley-dependent surface-state couplings and multiple possibilities of band orderings at two valleys that lead to various topological phases.

We compute a series of slabs up to 35 atomic layers to study the variance of the low-energy bands with the slab thickness. While the slab of less than 7 layers is metallic without a global band gap, the other slabs are insulators. Their gaps at both valleys and global gap are shown in Fig. 2(b), as functions of the (110) atomic layer number, n. The gaps at two valleys independently vary with thickness, due to strength changes of surface-state couplings. For X valley, the magnitude of the gap first decreases to nearly zero ($17 \leq n \leq 35$) and then increases ($7 \leq n \leq 15$) as the thickness decreases. In contrast, though there is a similar trend at R valley, the magnitude of the gap is always larger than 29 meV. Besides, we define the sign of the gaps, which becomes clear shortly.

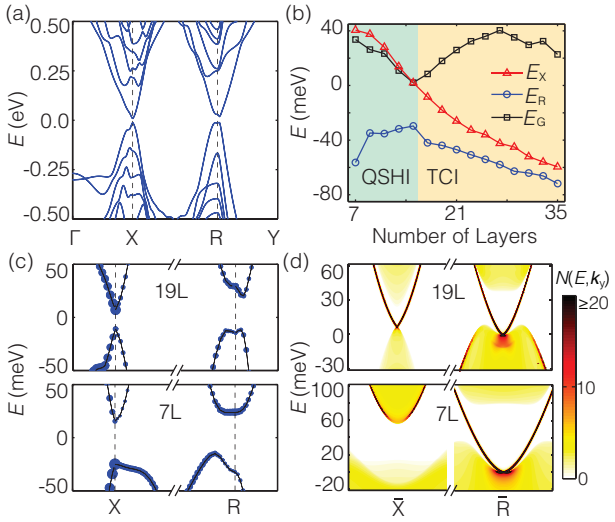

FIG. 2: Electronic structure of SnTe slabs. (a) Band structure of 19-layer slab. (b) The evolution of direct band gaps at two valleys, E_X and E_R, and the global gap, E_G, with the thickness of the slab. (c) Orbital resolved low-energy band structures of 19-layer (upper panel) and 7-layer (Lower) slabs. The size of blue circles is proportional to the orbital weight of Te ions. (d) The corresponding energy dispersion at the edge along y axis.

The closing and reopening of the band gap at X valley is possibly accompanied with the changes of the band ordering and corresponding band topology. To ascertain the band ordering, we first examine orbital-resolved band structures in Fig. 2(c). For 19-layer slab, p-orbitals of Te ions mainly contribute to the lowest conduction band states at both valleys, while the highest valence band states have few components from Te. The band ordering is consistent with the case of bulk SnTe, indicating band inversion compared with its atomic limit [12]. The inverted bands at both valleys suggest a possible two-dimensional topological crystalline insulator [6, 12]. For 7-layer slab, the orbitals from Te still contribute to the lowest conduction band states at R valley, while they move to the highest valence band states at X valley. Compared with 19-layer slab, the band exchange restores the band ordering of the atomic limit at X valley. Only one band inversion at R may lead to quantum spin Hall insulator [1, 2]. The sign of valley gaps in Fig. 2(b) is defined to distinguish band orderings, where the negative gap corresponds to inverted bands.

By calculating topological invariants [12, 24–26], we unambiguously confirm that the slabs with $n \geq 17$ and $7 \leq n \leq 15$ are respectively topological crystalline insulator and quantum spin Hall insulator (Details in Supplemental Material [14]). Besides, these confirmed topological crystalline insulators have a maximum global gap of 40 meV when $n = 27$. The maximum gap of quantum spin Hall insulators is 34 meV with $n = 7$. Due to

considerable gaps, topological phases can be expected at room temperature.

Symmetry-protected edge states are the defining characteristics of two-dimensional topological phases and lead to robust quantized conductance. Fig. 2(d) shows edge states of topological SnTe slabs. A topological crystalline insulator has two pairs of counter-propagating gapless Dirac edge modes within the band gap, as shown in energy dispersion of an edge along y axis. Two Dirac points are respectively located at high-symmetric momenta, $\bar{\mathrm{X}}$ ($k_y = 0$) and $\bar{\mathrm{R}}$ ($k_y = \pi$), which are projections of two valleys along y axis (Fig. 1(c)). These edge states are protected by in-plane mirror symmetry and contribute a robust quantized conductance of $2e^2/\hbar$ per edge. Besides, the edge-state couplings in nanoribbon arrays, which we will discuss later, are on the basis of the edge states. Similar edge states are also found at an edge along x axis [14]. For a quantum spin Hall insulator, the edge state has only one Dirac point at $\bar{\mathrm{R}}$, when R valley keeps band inversion. It is protected by time-reversal symmetry and gives a reduced quantized conductance of $e^2/\hbar$ per edge.

With the help of valley-contrasting couplings between surface states, two distinct types of topological phases are created in SnTe (110) slabs. Multiple topological phases in the same material system provide multi-mode quantum transport with good material compatibility. In contrast, a (001) slab harbors only two-dimensional topological crystalline insulator, due to only one independent valley [6, 27]. For a (111) slab, the absence of mirror symmetry excludes topological crystalline insulator and the band inversion is not found by first-principles calculations [14, 28], though it has symmetry-unrelated valleys [28–31].

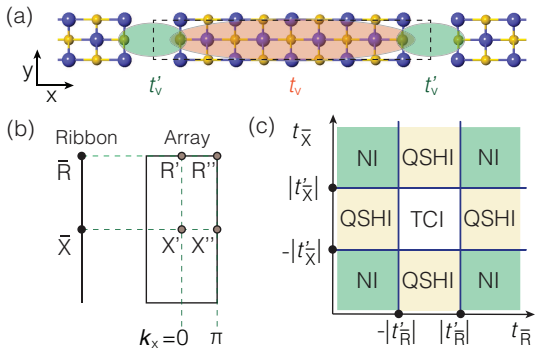

FIG. 3: Edge-state couplings in nanoribbon arrays. (a) Top view of a periodic array, where the vacuum layer is used as the spacer layer. The intra- and inter-nanoribbon couplings are respectively represented by red and green ellipses. The unit cell of the array is bounded by dashed lines. (b) When extending from a nanoribbon to an array, each valley becomes a doublet at time-reversal-invariant points of the Brillouin zone of the array. (c) Topological phase diagram of an array.

Edge-state couplings in a nanoribbon array.— Based on the above multivalley edge states in SnTe (110) slab, we further propose topological phase transitions in a nanoribbon array. Two-dimensional nanoribbon array is constructed by bottom-up design, with alternating one-dimensional SnTe nanoribbons and topological trivial spacer layers, as shown in Fig. 3(a). The edge states of the nanoribbon (Fig. 2(d)) give rise to the low-energy states of a nanoribbon array. Specific to an array with nanoribbon edges along y direction, time-reversal-invariant points, R′ and R″ (X′ and X″) in the Brillouin zone of the array are related to $\bar{\mathrm{R}}$ ($\bar{\mathrm{X}}$) valleys of the nanoribbon, as shown in Fig. 3(b). Compared with surface-state couplings in the slab, the coupling between edge states of the nanoribbon can occur through the spacer layer (inter-nanoribbon), besides the ones through the nanoribbon (intra-nanoribbon). It is noted that we can make an analogy between a nanoribbon array and a dimerized diatomic chain [32], where two edges of a nanoribbon correspond to two dimerized atoms. The two kinds of edge-state couplings are similar to staggered hopping amplitudes in the dimerized chain.

Taking into account two kinds of edge-state couplings, a low-energy Hamiltonian of the array immediately follows, $\mathcal{H}_v = \tau_x(t_v + t'_v \exp(ik_\perp))$, to study the band topology of the arrays. The Hamiltonian is also similar to that of the dimerized diatomic chain. Here, t_v and t'_v are respectively intra- and inter-nanoribbon coupling strengths. v is the index to distinguish $\bar{\mathrm{R}}$ and $\bar{\mathrm{X}}$ valleys. $\tau = \pm 1$ denote two edges of a nanoribbon. $k_\perp$ is the momentum perpendicular to the edge, while the dispersion along the parallel momentum is not considered. We assume the presence of inversion symmetry for simplicity and then two spins have the same copy of the above Hamiltonian. The gaps at $k_\perp = 0$ and π, obtained by diagonalizing the Hamiltonian, have magnitudes of $2|t_v + t'_v|$ and $2|t_v - t'_v|$, respectively. When $|t_v| = |t'_v|$, the band gap becomes zero at $k_\perp = 0$ or π, leading to a possible topological phase transition. Based on the number of band inversions and topological invariants [26], we have topological phase diagram of an array in Fig. 3(c), including both quantum spin Hall and topological crystalline insulators. When $|t_v| < |t'_v|$ for both valleys, the array is a topological crystalline insulator; $|t_v| > |t'_v|$ for both valleys leads to a normal insulator (NI); if $|t_v| < |t'_v|$ for one valley and $|t_v| > |t'_v|$ for the other, quantum spin Hall insulator emerges; $|t_v| = |t'_v|$ gives the boundary between topological phases.

Under the guidance of topological phase diagram, we compute the electronic properties of nanoribbon arrays by ab-initio tight-binding Hamiltonian [14]. A series of arrays with $n = 19$ are considered, where the variable nanoribbon width is used to tune intra-nanoribbon couplings. The number of (001) atomic layers, m, denotes the nanoribbon width and it is chosen to be odd to keep inversion symmetry. A vacuum layer of 6.4 Å is used as

the spacer layer. The model can also be seen as a sheet with a (001) atomic layer removed periodically. Fig. 4(a) shows a spin-degenerate band structure of an array. Four direct band gaps are located at R′, R″, X′ and X″. Based on the band gaps [14], Fig. 4(b) gives edge-state coupling strengths at two valleys and their evolution with the increasing nanoribbon width. The intra-nanoribbon couplings at both valleys continuously decrease as the nanoribbon width increases, while the couplings through the fixed vacuum layer are nearly unchanged. For the nanoribbon with $m \leq 31$, $|t_v| > |t'_v|$ at both valleys and the array is topological trivial. When the nanoribbon considered widens more than 31 layers, $|t_{\bar{\mathrm{R}}}|$ becomes smaller than $|t'_{\bar{\mathrm{R}}}|$, but $|t_{\bar{\mathrm{X}}}|$ is still larger than $|t'_{\bar{\mathrm{X}}}|$, leading to a topological phase transition from normal insulator to quantum spin Hall insulator. By further widening the nanoribbon, we expect a switch of coupling strengths at $\bar{\mathrm{X}}$ valley, similar to $\bar{\mathrm{R}}$. The array will be a topological crystalline insulator, in consistent with a perfect 19-layer slab, which can be regarded as the limit of infinite-width nanoribbons. The band topology is also confirmed by orbital-resolved bands and topological invariants [14].

Multiple topological phases are achieved by tuning the nanoribbon width. The vacuum layer width is another key parameter. The edge states decay exponentially when moving away the edge, so do their couplings through the vacuum layer. A wider/narrower vacuum layer therefore moves the lines of $|t'_v|$ downwards/upwards in Fig. 4(b) and have topological phase transition occur with a wider/narrower nanoribbon.

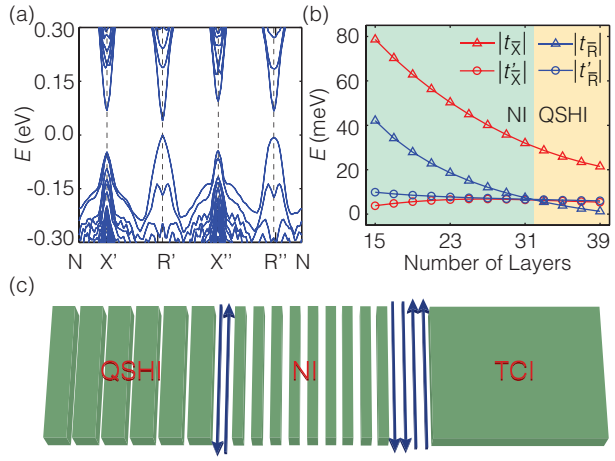

FIG. 4: Electronic structure of nanoribbon arrays. (a) A representative band structure of the array, with $m = 19$. The coordinates of N is $(\pi/2, \pi/2)$. (b) The evolution of coupling strengths with the nanoribbon width. (c) A schematic depiction of the arrays with various-width nanoribbon and vacuum layers. The nanoribbons and helical edge states are denoted by green blocks and blue arrows, respectively.

Discussion.— It is highly feasible to experimentally realize our proposed topological phases in nanoribbon arrays, with the help of fast-growing physical and chemical processes, e.g. lithography techniques [33–35]. As shown schematically in Fig. 4(c), well-patterned arrays harbor different topological non-trivial edge states at the phase boundary. The quantum phases and corresponding edge states are determined by the widths of nanoribbons and vacuum layers. The edge states with conductances of 0, $e^2/\hbar$ and $2e^2/\hbar$ per edge offer a dissipationless quantized transport of multiple stepwise variations, high tunability and good material compatibility, which has potential use in energy-efficient electronic and spintronic devices. Moreover, the spacer layer can be another materials, such as isostructural IV-VI semiconductors, PbTe and GeTe. Additional interactions from substrates and electric field can be introduced in the arrays. These methods possibly tune the edge-state couplings in a larger range.

These topological phases and their edge states in SnTe film system proposed above are very stable. Topological crystalline and quantum spin Hall insulators are respectively protected by mirror and time-reversal symmetries [1–3]. The quantized edge transport is therefore expected to be robust against the disorders that preserve corresponding symmetries. Though increasing temperature drives SnTe material class towards normal insulator [36], considerable gaps suggest topological non-trivial phases at high temperature, compared with existing two-dimensional topological insulators [4, 5]. While the additional doping shifts the chemical potential and introduces new characteristics, the band topology and non-trivial edge states can remain unchanged over a large concentration range, by reference to surface states of bulk SnTe [37, 38]. These topological properties are also expected to be kept under another perturbations, e.g. a moderate strain [12].

The mechanism of multivalley boundary-state couplings is rather versatile. A manifestation of the versatility is that the mechanism can be exploited in both top-down and bottom-up designs of two-dimensional topological phases, where the slab and nanoribbon array respectively give full play to surface-state and edge-state couplings. Moreover, the mechanism applies to a variety of exotic topological phases and materials.

Taking one step from topological crystalline and quantum spin Hall insulators, it immediately become compelling to apply multivalley boundary-state couplings to more exotic topological phases. Chern insulator and topological superconductor can be respectively realized by inducing magnetic and superconducting order into SnTe film system [38–41]. The valley-contrasting couplings between boundary states further lead to various (mirror) Chern numbers and multi-mode chiral edge states/Majorana zero modes. If the space layer is a superconductor and the electron-electron interaction is introduced, the structure of the nanoribbon array and multivalley boundary-state couplings have also potential use in realizing a two-dimensional sea of parafermions [11].

Besides, even if the system is away from topological phase transition and band gaps do not become inverted, tunable valley gaps (See Fig. 2(b)) are desirable in valley-selective optical and electronic applications [42–44].

It is noted that SnTe film system is an example of available materials. The versatile mechanism can also apply to another systems with multiple valleys, such as more IV-VI semiconductors [12, 45], elemental bismuth [26], ytterbium borides [46], transition metal chalcogenides [42, 43] and so on.

Conclusion.— In summary, valley-contrasting couplings between boundary states are studied in thin film system with symmetry-unrelated valleys, to design two-dimensional topological phases by top-down and bottom-up approaches. Both surface-state couplings in a slab and edge-state couplings in a nanoribbon array lead to quantum spin Hall insulator and topological crystalline insulator. In particular, topological phase transitions in an array can occur in a well-controlled way. The quantum transport of topological edge channels provides a set of quantized conductances. The mechanism broadens the scope of the research on topological materials.

This work is supported by China 973 Program (Projects 2013CB921900), DOE (DE-FG03-02ER45958, Division of Materials Science and Engineering) and Welch Foundation (F-1255).

[1] M. Z. Hasan and C. L. Kane, Rev. Mod. Phys. **82**, 3045 (2010).
[2] X.-L. Qi and S.-C. Zhang, Rev. Mod. Phys. **83**, 1057 (2011).
[3] Y. Ando and L. Fu, Annu. Rev. Con. Mat. Phys **6**, 361 (2015).
[4] M. König, S. Wiedmann, C. Brüne, A. Roth, H. Buhmann, L. W. Molenkamp, X.-L. Qi, and S.-C. Zhang, Science **318**, 766 (2007).
[5] I. Knez and R.-R. Du, Front. Phys. **7**, 200 (2012).
[6] J. Liu, T. H. Hsieh, P. Wei, W. Duan, J. Moodera, and L. Fu, Nat. Mater. **13**, 178 (2014).
[7] H. Ozawa, A. Yamakage, M. Sato, and Y. Tanaka, Phys. Rev. B **90**, 045309 (2014).
[8] E. O. Wrasse and T. M. Schmidt, Nano Lett. **14**, 5717 (2014).
[9] L. Fu and C. L. Kane, Phys. Rev. Lett. **100**, 096407 (2008).
[10] R. Yu, W. Zhang, H.-J. Zhang, S.-C. Zhang, X. Dai, and Z. Fang, Science **329**, 61 (2010).
[11] J. Klinovaja and D. Loss, Phys. Rev. B **90**, 045118 (2014).
[12] T. H. Hsieh, H. Lin, J. Liu, W. Duan, A. Bansil, and L. Fu, Nat. Commun. **3**, 982 (2012).
[13] J. Liu, W. Duan, and L. Fu, Phys. Rev. B **88**, 241303 (2013).
[14] See Supplemental Material for methods, the calculations of topological invariants of SnTe slabs, edge states along x axis of SnTe slabs, (111) SnTe slabs and band evolution of nanoribbon arrays, which includes Refs. [15-21]. .
[15] G. Kresse and J. Furthmüller, Phys. Rev. B **54**, 11169 (1996).
[16] G. Kresse and D. Joubert, Phys. Rev. B **59**, 1758 (1999).
[17] J. P. Perdew, K. Burke, and M. Ernzerhof, Phys. Rev. Lett. **77**, 3865 (1996).
[18] N. Marzari and D. Vanderbilt, Phys. Rev. B **56**, 12847 (1997).
[19] I. Souza, N. Marzari, and D. Vanderbilt, Phys. Rev. B **65**, 035109 (2001).
[20] M. L. Sancho, J. L. Sancho, and J. Rubio, J. Phys. F: Met. Phys. **14**, 1205 (1984).
[21] X. Li, H. Liu, H. Jiang, F. Wang, and J. Feng, Phys. Rev. B **90**, 165412 (2014).
[22] B. Zhou, H.-Z. Lu, R.-L. Chu, S.-Q. Shen, and Q. Niu, Phys. Rev. Lett. **101**, 246807 (2008).
[23] H.-Z. Lu, W.-Y. Shan, W. Yao, Q. Niu, and S.-Q. Shen, Phys. Rev. B **81**, 115407 (2010).
[24] T. Fukui, Y. Hatsugai, and H. Suzuki, J. Phys. Soc. Jpn. **74**, 1674 (2005).
[25] T. Cai, X. Li, F. Wang, S. Ju, J. Feng, and C.-D. Gong, Nano Lett. **15**, 6434 (2015).
[26] L. Fu and C. L. Kane, Phys. Rev. B **76**, 045302 (2007).
[27] G. Yang, J. Liu, L. Fu, W. Duan, and C. Liu, Phys. Rev. B **89**, 085312 (2014).
[28] Y. Shi, M. Wu, F. Zhang, and J. Feng, Phys. Rev. B **90**, 235114 (2014).
[29] X. Li, F. Zhang, Q. Niu, and J. Feng, Sci. Rep. **4**, 6397 (2014).
[30] J. Liu and L. Fu, Phys. Rev. B **91**, 081407 (2015).
[31] S. Safaei, M. Galicka, P. Kacman, and R. Buczko, New J. Phys. **17**, 063041 (2015).
[32] W. P. Su, J. R. Schrieffer, and A. J. Heeger, Phys. Rev. Lett. **42**, 1698 (1979).
[33] M. A. Walsh and M. C. Hersam, Annu. Rev. Phys. Chem. **60**, 193 (2009).
[34] J. G. Son, M. Son, K.-J. Moon, B. H. Lee, J.-M. Myoung, M. S. Strano, M.-H. Ham, and C. A. Ross, Adv. Mater. **25**, 4723 (2013).
[35] H. Suzuki, T. Kaneko, Y. Shibuta, M. Ohno, Y. Maekawa, and T. Kato, Nat. Commun. **7**, 11797 (2015).
[36] P. Dziawa et al., Nat. Mater. **11**, 1023 (2012).
[37] I. Pletikosić, G. D. Gu, and T. Valla, Phys. Rev. Lett. **112**, 146403 (2014).
[38] C. M. Polley, V. Jovic, T.-Y. Su, M. Saghir, D. Newby, B. J. Kowalski, R. Jakiela, A. Barcz, M. Guziewicz, T. Balasubramanian, et al., Phys. Rev. B **93**, 075132 (2016).
[39] C. Fang, M. J. Gilbert, and B. A. Bernevig, Phys. Rev. Lett. **112**, 046801 (2014).
[40] C. Fang, M. J. Gilbert, and B. A. Bernevig, Phys. Rev. Lett. **112**, 106401 (2014).
[41] B. A. Assaf, F. Katmis, P. Wei, C.-Z. Chang, B. Satpati, J. S. Moodera, and D. Heiman, Phys. Rev. B **91**, 195310 (2015).
[42] X. Li, T. Cao, Q. Niu, J. Shi, and J. Feng, Proc. Natl. Acad. Sci. USA **110**, 3738 (2013).
[43] J. Qi, X. Li, Q. Niu, and J. Feng, Phys. Rev. B **92**, 121403 (2015).
[44] H. Jiang, H. Liu, J. Feng, Q. Sun, and X. C. Xie, Phys. Rev. Lett. **112**, 176601 (2014).
[45] Y. Sun, Z. Zhong, T. Shirakawa, C. Franchini, D. Li,

Y. Li, S. Yunoki, and X.-Q. Chen, Phys. Rev. B **88**, 235122 (2013).
[46] H. Weng, J. Zhao, Z. Wang, Z. Fang, and X. Dai, Phys. Rev. Lett. **112**, 016403 (2014).